

Compressible plume dynamics and stability

By MARK PETER RAST

High Altitude Observatory, National Center for Atmospheric Research, PO Box 3000,
Boulder, CO 80307-3000, USA

(Received 10 June 1997 and in revised form 17 March 1998)

This paper presents a numerical study of the dynamics and stability of two-dimensional thermal plumes in a significantly stratified layer. Motivated by stellar envelope convection in which radiative cooling at the star's photosphere drives vigorous downflows, we examine cool plumes descending through an adiabatically stratified layer of increasing density with depth. Such flows are inaccessible by laboratory experiments, yet are important to the understanding of heat and momentum transport, magnetic field generation, and acoustic excitation in stars like the Sun. We find that the structure of thermal plumes in a stratified compressible medium is significantly different from that in an incompressible one, with pressure perturbations playing an important dynamical role. Additionally, we find that the plumes are subject to vigorous secondary instabilities even in a quiescent background medium. While the flows studied are not fully turbulent but transitional, the nature of the compressive instabilities and their influence on subsequent flow evolution suggests that advective detrainment of fluid from the plume region results. Simplified plume models assuming a hydrostatic pressure distribution and velocity-proportional entrainment may thus be inappropriate in this context.

1. Introduction

Thermal plume generation and interaction is important to the the dynamics of and heat transport by thermal convection in a variety of settings (cf. Turner 1986; Zocchi, Moses & Libchaber 1990). The work presented here is most fundamentally motivated by studies of compressible convection. Those focusing specifically on compressibility and employing an ideal-gas equation of state (Graham 1977; Hurlburt, Toomre & Massaguer 1984; Cattaneo *et al.* 1991) have clearly demonstrated the importance of flow asymmetry (fast narrow downdraughts and broader gentler upflows) to the dynamics and heat transport properties of thermal convection in a stratified medium. The asymmetry arises because positive pressure perturbations in both the upflow and downflow regions contribute positively to density perturbations, enhancing buoyancy driving in the downflows but contributing to buoyancy braking of the upflows (Massaguer & Zahn 1980; Hurlburt *et al.* 1984). Mean stratification of the fluid necessitates compression of the downflowing and expansion and overturning of the upflowing material. Other work has looked at compressible convection in non-ideal ionizing gases (Stein & Nordlund 1989; Rast *et al.* 1993; Rast & Toomre 1993*a, b*), a setting appropriate to stellar envelopes. In those studies, strong radiative cooling and diffusive boundary layer instabilities were found to generate particularly vigorous new downflow plumes whose strength at depth is maintained by the increased specific heat of the fluid upon partial ionization. This apparent propensity toward downflow plumes in compressible convective flows has inspired a number of authors to consider them

as an essential ingredient in understanding the thermal stratification of the overshoot region below the solar convection zone and possible magnetic dynamo mechanisms operating there (e.g. Schmitt, Rosner & Bohn 1984; Simon & Weiss 1991; Zahn 1991; Parker 1993; Charbonneau & MacGregor 1997). But do the downflow plumes generated at the solar surface actually descend through the entire depth of the solar convection zone and penetrate below? Previous authors (Schmitt *et al.* 1984; Simon & Weiss 1991; Rieutord & Zahn 1995) have answered this in the affirmative based on simplified stratified but incompressible (small pressure fluctuations) plume models incorporating velocity-proportional entrainment. Here we examine, via direct numerical simulation, the dynamics and stability of fully compressible downflow plumes in a significantly stratified medium, and find that such plumes are subject to vigorous secondary instabilities leading to plume disruption. Pressure fluctuations play an important dynamical role, initiating the detachment of vortex pairs which leave the plume region. While the flows we study are not fully turbulent but transitional, the nature of these instabilities and the subsequent evolution of the flow suggest that *detrainment* rather than entrainment of fluid from the plume region results. This is quite contrary to what is assumed in simplified plume models, and is a direct consequence of compression and isolation of shed vortex pairs rather than their expansion and interaction as observed in incompressible or upward-directed compressible plume flows.

The remainder of this paper is organized as follows. The model is formulated in the next section, including a description of the polytropic background state, boundary conditions, and numerical method. In §3 we describe the single downflow plume solutions obtained and discuss their dynamics and stability. Emphasis is placed on the onset of instability in a quiescent background. In §4 we contrast these results with solutions involving multiple plume interactions and upward directed plumes, and discuss possible implications for more fully developed turbulent flows. We conclude in §5 by briefly connecting the work back to some of its astrophysical motivations.

2. Model

We consider thermal plumes penetrating an adiabatically stratified two-dimensional plane-parallel layer of ideal gas. The fluid is confined between stress free and impenetrable horizontal boundaries and within a horizontally periodic domain. The temperature T is held constant on the upper and lower boundaries. The unperturbed atmosphere is polytropic, meaning that the pressure P and density ρ are related by

$$\frac{d \ln P}{d \ln \rho} = \frac{m + 1}{m}, \quad (1)$$

with the polytropic index m constant throughout (cf. Cox & Giuli 1968). Equation (1), along with hydrostatic balance, constant gravity, and an ideal gas equation of state, implies a linear temperature profile with depth z , and density and pressure which scale with temperature as m and $m + 1$ respectively (figure 1*a*). Additionally, adiabatic stratification and thus neutral convective stability in a monatomic ideal gas requires $m = 1.5$. Thus the structure of the unperturbed atmosphere is determined solely by the temperature gradient θ .

Convenient measures of density and pressure stratification are the local scale heights, H_ρ and H_P respectively. In a polytropic atmosphere these are increasing

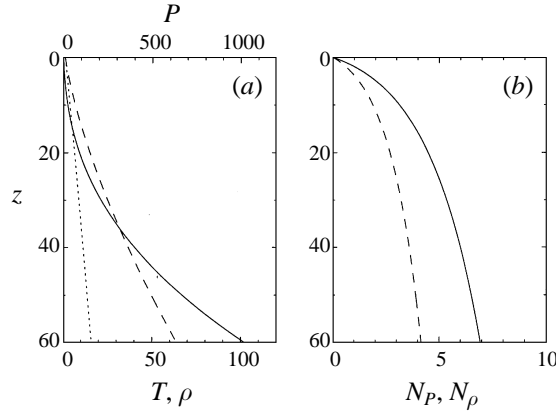


FIGURE 1. Stratification of the unperturbed atmosphere: (a) temperature T (dotted line), density ρ (dashed curve) and pressure P (solid curve) and (b) number of density scale heights N_ρ (dashed curve) and pressure scale heights N_P (solid curve) spanned as a function of depth z .

linear functions of temperature, and the total number of scale heights spanned,

$$N_\rho = \int_0^z H_\rho^{-1} dz = \int_0^z \frac{1}{\rho} \frac{d\rho}{dz} dz = m \ln(T) \quad (2)$$

and

$$N_P = \int_0^z H_P^{-1} dz = \int_0^z \frac{1}{P} \frac{dP}{dz} dz = (m+1) \ln(T), \quad (3)$$

increases most rapidly with depth near the top and more slowly near the bottom of the stratified layer (figure 1b). In this paper we considered atmospheres up to 7 pressure (or 4 density) scale heights deep. The pressure and density ratios across such layers are correspondingly 1024 and 64.

To the above described quiescent polytropic atmosphere we apply a Gaussian temperature perturbation. The perturbation is generally cool and centred along the upper boundary, although warm perturbations at the bottom and multiple perturbations are briefly considered as well. Density along the boundary is chosen initially to satisfy pressure equilibrium, but subsequently evolves unfettered. Motions ensue within the domain as the thermal anomaly diffusively spreads inward from the boundary, inducing buoyancy forces and horizontal pressure gradients. The motions are of course governed by the equations of mass, momentum, and energy conservation, and we express these in a non-dimensional form. Temperature and density are scaled by the unperturbed values T_0 and ρ_0 at the top of the domain. Length is measured in units of the full width at half the maximum of the applied Gaussian temperature perturbation d , and the unit of time is taken to be the isothermal sound travel time over that distance at the unperturbed upper boundary temperature $d/(RT_0)^{1/2}$. We define two dimensionless numbers: a sound speed Reynolds number,

$$Re = \frac{\rho_0 d (RT_0)^{1/2}}{\mu}, \quad (4)$$

and a Prandtl number

$$Pr = \frac{\mu R}{k}. \quad (5)$$

In the Prandtl number so defined the gas constant R replaces the usual occurrence of

the specific heat C_v for ease of generalization to non-ideal fluids in which C_v is not constant. Since this study is confined to ideal gases only, the true Prandtl number, the ratio of thermal to viscous diffusion times, is simply a constant multiple ($C_v/R = 3/2$) of Pr . Similarly, the isothermal sound speed was chosen in the definition of the Reynolds number (4) as it is independent of the specific heat, whereas the adiabatic sound speed given by $(\gamma RT)^{1/2}$ depends on the ratio $\gamma = C_p/C_v$ (equal to $5/3$ in an ideal gas).

With these scalings and definitions we write the non-dimensional equations as

$$\frac{\partial \rho}{\partial t} = -\frac{\partial(\rho u_k)}{\partial x_k}, \quad (6)$$

$$\frac{\partial(\rho u_j)}{\partial t} = -\frac{\partial(\rho u_j u_k)}{\partial x_k} - \frac{\partial P}{\partial x_j} + \frac{1}{Re} \left[\frac{\partial^2 u_j}{\partial x_k \partial x_k} + \frac{1}{3} \frac{\partial}{\partial x_j} \left(\frac{\partial u_k}{\partial x_k} \right) \right] + K_2 \rho \delta_{j3}, \quad (7)$$

and

$$\begin{aligned} \frac{\partial T}{\partial t} = & -u_k \frac{\partial T}{\partial x_k} - \frac{T}{C_v} \frac{\partial u_k}{\partial x_k} + \frac{1}{Re Pr} \frac{1}{\rho C_v} \frac{\partial^2 T}{\partial x_j \partial x_j} \\ & + \frac{1}{Re} \frac{1}{\rho C_v} \left[\left(\frac{\partial u_k}{\partial x_j} + \frac{\partial u_j}{\partial x_k} \right) \frac{\partial u_j}{\partial x_k} - \frac{2}{3} \left(\frac{\partial u_k}{\partial x_k} \right)^2 \right], \end{aligned} \quad (8)$$

where $K_2 = dg/RT_0 = (m+1)\theta$ (equal to the ratio of d/H_p at the top of the layer) measures gravity and P is given by the ideal gas law $P = \rho T$. Note that both the dynamic viscosity μ and thermal conductivity k are taken as constants, and that the bulk viscosity is assumed zero. This means of course that the kinematic viscosity $\nu = \mu/\rho$ and the thermal diffusivity $\kappa = k/\rho C_v$ vary with fluid density, decreasing with increasing density and therefore depth. Also note that, since depth z is measured downward in the direction of gravity, downward velocities are positive.

Two-dimensional initial value solutions to the above nonlinear equations were computed using fully explicit second-order finite difference techniques, centred in the interior and one-sided on the boundaries. Such second-order differencing lends itself to rapid communications on the parallel architecture of the Connection Machine CM-5 used for these studies, and calculations of very high spatial resolution on 1024^2 , 1024×2048 , and 1472^2 grids were possible. The resolution was enhanced in the plume region by an arc-tangent transformation from the regular computational grid to an irregular sampling in physical space. Such grid stretching permitted domain sizes of up to $60d$ squared while maintaining fine gridding in the flow region. The large domains minimize lateral boundary influences and allowed study of plume dynamics in an effectively infinite half-space (computations were terminated before the plume impacted the opposite boundary from its origin). The resolution so obtained by this combination of fine and non-uniform gridding permitted over 30 grid points per Taylor microscale in the least viscous most evolved solutions, and many more in less evolved or more viscous ones. The equations were time-advanced using an Adams–Bashforth scheme (Richtmyer & Morton 1967), the weak unconditional instability inherent in such a scheme posing no difficulty due to the initial value nature of the problem. Resolution checks on both uniform and non-uniform grids were made, verifying at least internal consistency. Moreover, the code is a direct adaptation of a previous compressible convection code, with that code having been checked both for linear growth and against a pseudospectral calculation (cf. Rast 1991, 1992).

| Case | Re | Pr | Pc | $\Delta x (\times 10^2)$ | $\Delta z (\times 10^2)$ | λ | R_λ | F_h |
|------|------|------|--------|--------------------------|--------------------------|-----------|-------------|-------|
| A | 75 | 0.13 | 10.0 | 1.20–1.78 | 3.25–16.2 | 0.427 | 47.9 | 0.368 |
| B1* | 100 | 0.1 | 10.0 | 1.20–1.78 | 3.25–16.2 | 0.393 | 60.4 | 0.383 |
| B2 | 100 | 0.5 | 50.0 | 1.20–1.78 | 3.25–16.2 | 0.310 | 35.3 | 0.146 |
| B3 | 100 | 1.0 | 100.0 | 1.20–1.78 | 3.25–16.2 | 0.302 | 29.4 | 0.093 |
| C | 125 | 0.08 | 10.0 | 1.20–1.78 | 3.25–16.2 | 0.371 | 73.6 | 0.393 |
| D* | 150 | 0.06 | 10.0 | 0.798–1.67 | 1.08–5.41 | 0.348 | 91.1 | 0.432 |
| E* | 200 | 0.05 | 10.0 | 0.798–1.67 | 1.08–5.41 | 0.324 | 116.0 | 0.444 |
| F1* | 250 | 0.04 | 10.0 | 0.798–1.67 | 1.08–5.41 | 0.310 | 141.0 | 0.454 |
| F2 | 250 | 0.01 | 2.5 | 0.798–1.67 | 1.08–5.41 | 0.486 | 228.0 | 0.696 |
| F3 | 250 | 0.1 | 25.0 | 0.798–1.67 | 1.08–5.41 | 0.244 | 99.8 | 0.283 |
| F4 | 250 | 1.0 | 250.0 | 0.798–1.67 | 1.08–5.41 | 0.188 | 47.2 | 0.063 |
| F5 | 250 | 5.0 | 1250.0 | 0.798–1.67 | 1.08–5.41 | 0.199 | 30.4 | 0.021 |
| F6 | 250 | 10.0 | 2500.0 | 0.277–1.50 | 1.35 | 0.200 | 28.5 | 0.016 |

TABLE 1. Parameters of the numerical experiments. Those experiments marked with an asterisk were conducted both with quiescent and perturbed initial conditions.

3. Single-plume structure, dynamics, and stability

In this section we present the results of three series of numerical experiments summarized in table 1. The studies were designed to explore variations in plume dynamics with Reynolds and Prandtl number while holding remaining parameters such as background stratification ($\theta = 0.25$) and applied temperature perturbation (minimum temperature along the upper boundary $0.3T_0$) fixed. Note that Re quoted in table 1 is a scaling parameter based on fluid properties at the top of the domain. Due to fluid stratification, values of this parameter would exceed those quoted by a factor of several hundred if it were based on fluid properties in the lower portion of the domain. The actual vigour of the resulting flows is thus poorly represented by the numerical value of Re , and the microscale Reynolds number R_λ determined from the solutions (see § 3.1) is quoted in table 1 as well.

Resolution requirements of the simulations listed in table 1 varied: Cases A–C were computed on a 1024×1024 stretched grid covering a 60×60 domain, while Cases D–F5 utilized a 1024×2048 stretched grid over a 40×40 domain. The highest Prandtl number case, F6, was computed within a restricted domain of 20×20 on a 1472×1472 stretched grid. Minimum and maximum values of the grid spacing Δx and Δz within 3 units either side of the plume centre are given in table 1 to indicate the actual resolution achieved by non-uniform gridding. Note that the plume occupies only the central region of even this subdomain (see figure 3) where Δx is the smallest and thus the resolution is the finest.

3.1. Parameters

The numerical experiments conducted comprise three series: Series A consisting of A, B1, C–F1, Series B of B1–B3, and Series F of F1–F6. For Series A the product of the Prandtl and Reynolds numbers, the Péclet number Pc , was held constant while varying both Re and Pr . This effectively adjusts the dynamic viscosity of the fluid while holding the thermal conductivity constant. Series B and F allow the Péclet number to vary with the Prandtl number while holding Re constant at two different values, 100 and 250 respectively. Series A consists entirely of low Prandtl number

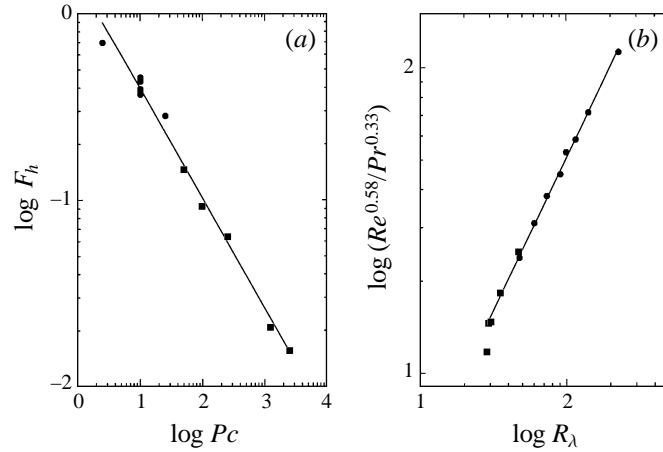


FIGURE 2. (a) The enthalpy flux measured at a depth of one density scale height as a function of Péclet number Pc , and (b) the scaling of the microscale Reynolds number R_λ with Reynolds Re and Prandtl Pr numbers. Low Prandtl number cases and high Prandtl number cases are shown with filled circles and squares respectively.

solutions, those of most relevance to astrophysical convection, while B and F include some higher Prandtl number comparisons.

The vigour of each of the solutions is indicated by entries in the last two columns of table 1. While all the experiments are initially adiabatic in the interior and are subject to the same applied temperature perturbation on the boundary, those of lowest Péclet number allow greatest surface cooling at the plume site. Fluid moves out of a thermal boundary layer of thickness δ on a buoyancy time scale $t_b^2 \sim \delta \rho / (\rho' g)$, where primed quantities are fluctuations about the horizontal mean. Diffusive loss of heat results in temperature fluctuations of magnitude $T'/T \sim t_b/t_\kappa$, where $t_\kappa = \delta^2/\kappa$ is the characteristic thermal diffusion time. As the Péclet number increases (κ decreases) the thermal diffusion time increases relative to the buoyancy time. The fluid moves out of the thermal boundary layer having cooled only little, and the resultant plumes are weaker and narrower than they are at lower values of Pc . The enthalpy flux (table 1, column 9),

$$F_h = -\frac{5}{2} \int \rho w T' dx, \quad (9)$$

defined to be positive when directed upward (as in a cool downflow plume) and measured at a depth of one density scale height, reflects this, scaling empirically as $F_h \sim Pc^{-0.59}$. This is illustrated by figure 2(a), which also suggests that the scaling at low Prandtl numbers (values plotted with filled circles) may differ slightly from that at the higher ones (values plotted with filled squares). Note that the enthalpy flux carried by a thermal plume in a stratified medium is not constant with depth. For adiabatic motions T'/T remains constant. Thus, as the fluid is gravitationally accelerated downward the magnitudes of both T' and ρw increase with depth, and consequently so does F_h . In these simulations the motions are not adiabatic. Formed on a diffusive scale, the plumes suffer horizontal losses even at very low values of κ . The losses are most significant in the upper layers of the domain where the temperature gradients are sharpest and the density is lowest (thus the diffusivity is highest). Despite this F_h increases with depth, albeit more slowly than in an adiabatic flow, with gravitational acceleration of the fluid more than compensating for the

reduction in temperature perturbation amplitude. Also note that the flux carried by the plumes in these simulations in all cases far exceeds that carried conductively by the adiabatic background (given by θ/Pr). Additionally, variation of the mean state due to plume formation is small because of the large domain sizes considered. Thus the plumes studied here should be considered strong, isolated, and embedded in an adiabatic domain.

Another measure of plume vigour is the microscale Reynolds number, $R_\lambda = u_m \lambda / \nu$ (table 1, column 8). Here $\lambda = (\langle u^2 \rangle / \langle \omega^2 \rangle)^{1/2}$ measures the characteristic horizontal extent of the shear at each depth (ω being the only surviving component of the vorticity in two dimensions and the angled brackets indicating horizontal mean values), the characteristic velocity of the flow u_m is taken to be the flow speed $(u^2 + w^2)^{1/2}$ averaged over the shear region of size λ in the plume centre, and the kinematic viscosity ν varies with depth as the background polytropic density. The values of λ and R_λ quoted in table 1 are measured at a depth of one density scale height immediately before the onset of sinuous instability anywhere along the stem. As illustrated by figure 2(b), R_λ scales empirically as

$$R_\lambda \sim Re^{0.58} Pr^{-0.33}, \quad (10)$$

and again there is an indication that the scaling may differ between the higher (plotted as filled squares) and lower (plotted as filled circles) Prandtl number cases. Additionally, there is a general increase in R_λ with depth at all Prandtl numbers and the scaling with Re and Pr given by (10) holds *independent of depth* for low Prandtl number stem flow (this depth independence does not hold for the high Pr cases). Note that the values of R_λ cited in table 1 and plotted in figure 2(b) are representative of the stem flow before instability. Significantly higher values are characteristic of the deeper cap structure and the intricate dynamics which develop subsequent to the onset of instability.

3.2. Early flow development at low and high Prandtl numbers

Early stages in the development of a typical low Prandtl number solution (Case B1) are illustrated in figure 3 with a series of images of the horizontal vorticity. Each frame encompasses about 1/10th of the horizontal and the full vertical extent of the computational domain. In the early stages of development, the flow shares the general cap and stem morphology common to laminar starting plumes in incompressible media (e.g. Moses, Zocchi, & Libchaber 1993 and references therein). Subsequently the stem is subject to a symmetric pinch-like instability which detaches the leading vortex pair. This type of instability is not seen in Boussinesq thermal plumes or, as will be seen in §4, in fully compressible upflowing plumes. Great care was taken in these calculations to ensure very low levels of numerical noise. Under such conditions the symmetric pinch-like instability generally occurs twice before small differences between the strengths of the left-hand and right-hand vortices grow sufficiently to destabilize the stem in a sinuous mode (not illustrated by figure 3 but illustrated and discussed further in §3.5). Growth of the sinuous mode can be facilitated by random temperature perturbations in the initial conditions or multiple plume interactions. Either of these serves to destabilize the delicate balance unique to precisely equal-magnitude cap vortices. Those experiments marked with an asterisk in table 1 were conducted twice, once with quiescent initial conditions and once with added random background temperature perturbations of amplitude 10^{-3} . Those experiments in table 1 without an asterisk were initiated only with the quiescent state. We discuss the solutions resulting from quiescent initial conditions further in this and the following

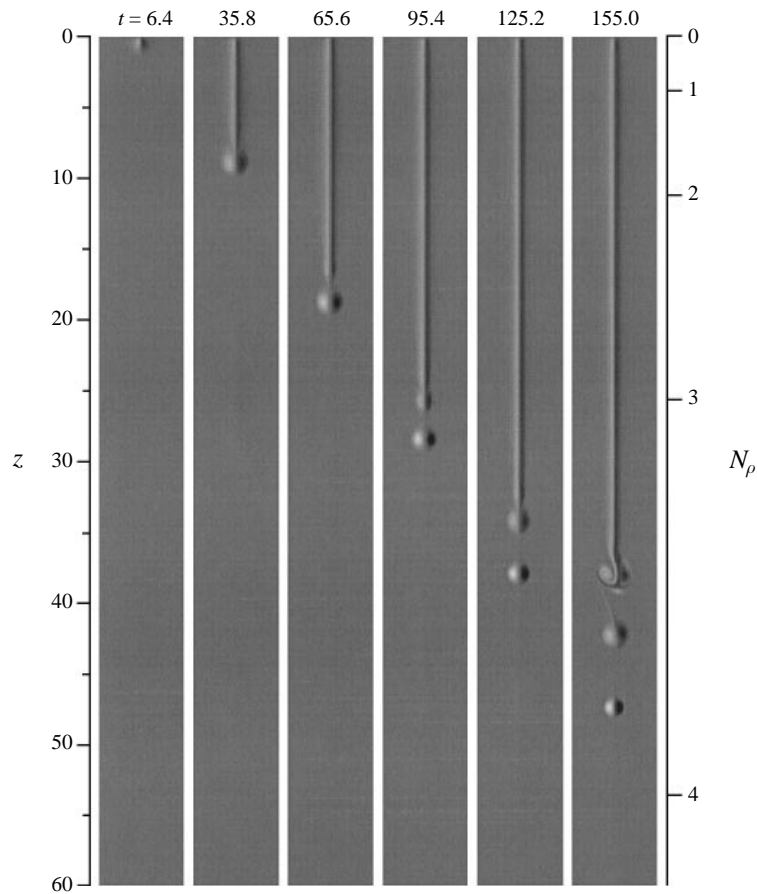


FIGURE 3. A series of horizontal vorticity images (light and dark being oppositely signed vorticity) for a typical low Prandtl number solution (Case B1). The full vertical extent and 1/10 the horizontal extent (6 units) of the computational domain is shown in each image.

two sections, leaving discussion of the sinuous instability mode and the more evolved turbulent flows for §§ 3.5 and 4.

Early development of a high Prandtl number solution (Case F6) is illustrated in figure 4 which displays temperature fluctuations about the horizontal mean. Here a very narrow plume develops out of the coolest central portion of the applied Gaussian perturbation. The thermal diffusivity in this case is greatly reduced ($Pc = 2500$), and persistent temperature structures form within the vortex cap. Flow dynamics are dominated by local temperature variations, with animated sequences of images showing the cool fluid descending down the plume centre, returning along the outside of the head, then stagnating at the rear of the cap, before finally descending a second time to form the intricate windings apparent in figure 4. Persistent positive temperature fluctuations (light regions in figure 4) develop early as a result of compressional heating. This relatively warm and buoyant fluid descends less rapidly than the cool fluid surrounding it and ultimately comes to occupy the central portion of the loosely wound vortex pair. The high spatial resolution required to resolve these intricate temperature variations and fluid motions places severe constraints on the total spatial extent of the experiment. Only the shallow domain 20 units deep

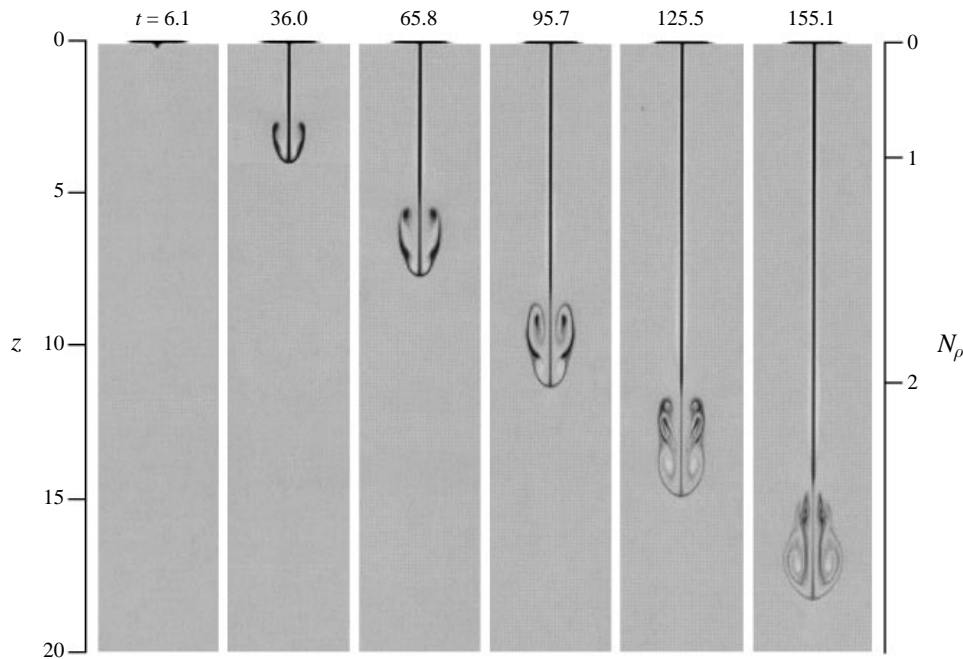


FIGURE 4. A series of temperature perturbation images (light indicating temperatures above and dark temperatures below the horizontal mean) for a high Prandtl number solution (Case F6). The full vertical extent and $1/5$ the horizontal extent (4 units) of the computational domain is shown in each image. Note that in this case the plume emerges from only the very central portion of the applied Gaussian temperature perturbation.

illustrated in figure 4 could be considered with adequate resolution for $Pr = 10.0$. As a consequence of both this limited depth and the quiescent initial conditions, the secondary instabilities which dominate the later stages of the deep low Prandtl number simulations did not have time to develop in Case F6 before the bottom of the domain was encountered by the flow. Note however that after descent to a comparable depth the plume in the low Prandtl number solution of figure 3 is also only just beginning to show signs of the pinch instability. Furthermore, *all* solutions computed in deeper domains, independent of Prandtl number, exhibited vigorous secondary instabilities. This is true even of Case F5 with $Pr = 5$ which displayed early evolution similar to that of Case F6 but subsequently exhibited head consolidation and then pinch and sinuous instability in the lower half of the domain. We thus expect that the pinch and sinuous flow instabilities we examine in detail in this paper occur in all compressible downflow plumes, independent of Pr , given a sufficiently deep and stratified background.

3.3. Stem flow before instability onset

When considered in detail the laminar stem flow exhibited by these compressible starting plumes is quite unique. Figure 5 plots horizontal cross-sections of the stem flow velocity and temperature fluctuations at three depths in Case D: $N_\rho = 0.5$, $N_\rho = 1.0$, and $N_\rho = 2.5$ corresponding to $z = 1.57$, $z = 3.80$, and $z = 17.2$ respectively. The flow, particularly in the uppermost layers, exhibits the curious property that the upflow velocity peaks sharply immediately adjacent to the downflow plume. This is in contrast to motion exhibited by either compressible or incompressible cellular

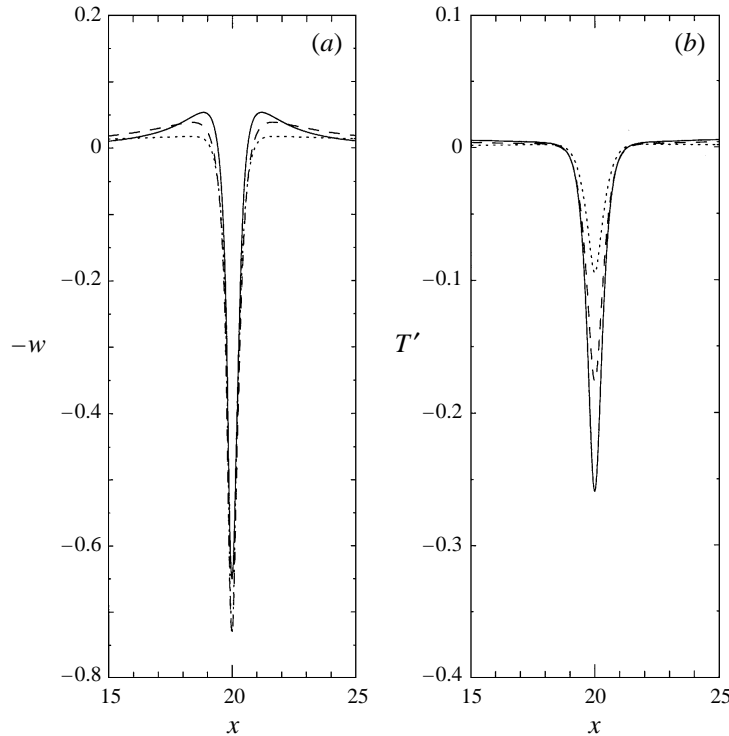


FIGURE 5. Horizontal cuts of (a) vertical velocity $-w$ (upflow positive) and (b) temperature perturbations T' at three depths in Case D: $N_\rho = 0.5$ (solid curve), $N_\rho = 1$ (dashed curve), and $N_\rho = 2.5$ (dotted curve) corresponding to $z = 1.57$, $z = 3.80$, and $z = 17.2$ respectively. All cuts sample nearly steady plume stem flow, and in both figures only one quarter of the full horizontal extent of the computational domain is shown.

Rayleigh–Bénard convection in which predominantly horizontal motions are found adjacent to the site of downflow. In those settings bottom heating plays an important dynamical role. Here the influence of the lower boundary is absent or extremely weak, and the upflows are driven locally in response to buoyancy forces and large pressure gradients induced in the vicinity of the downflow plume. Figure 6 plots the pressure perturbations and the associated Mach number of the flow in the upper layers of the fluid. Pressure perturbations are positive in the central core of the plume where the flow is convergent, the horizontal velocity vanishes, and the vertical Mach number peaks. Adjacent to the core flow, high Mach number horizontal flow and strong negative pressure fluctuations occur. It is in response to the direct pressure gradients and induced buoyancy forces in this outer region that the fluid is accelerated upward and inward before descending down the plume stem.

Figure 7 plots the plume stem diameter d as a function of depth for the experiments comprising Series A before the onset of sinuous instability. The diameter is measured as the distance between oppositely signed vorticity maxima on either side of the plume. (Note that the plumes are strictly two-dimensional and not axisymmetric.) Thick vertical bars in the figure are composed of individual data points, and the jumps in value with depth reflect twice the horizontal grid spacing in the domain (the positions of the vorticity maxima each shift discretely by one grid point as the plume diameter changes). Thin solid curves in figure 7 plot the best power-law

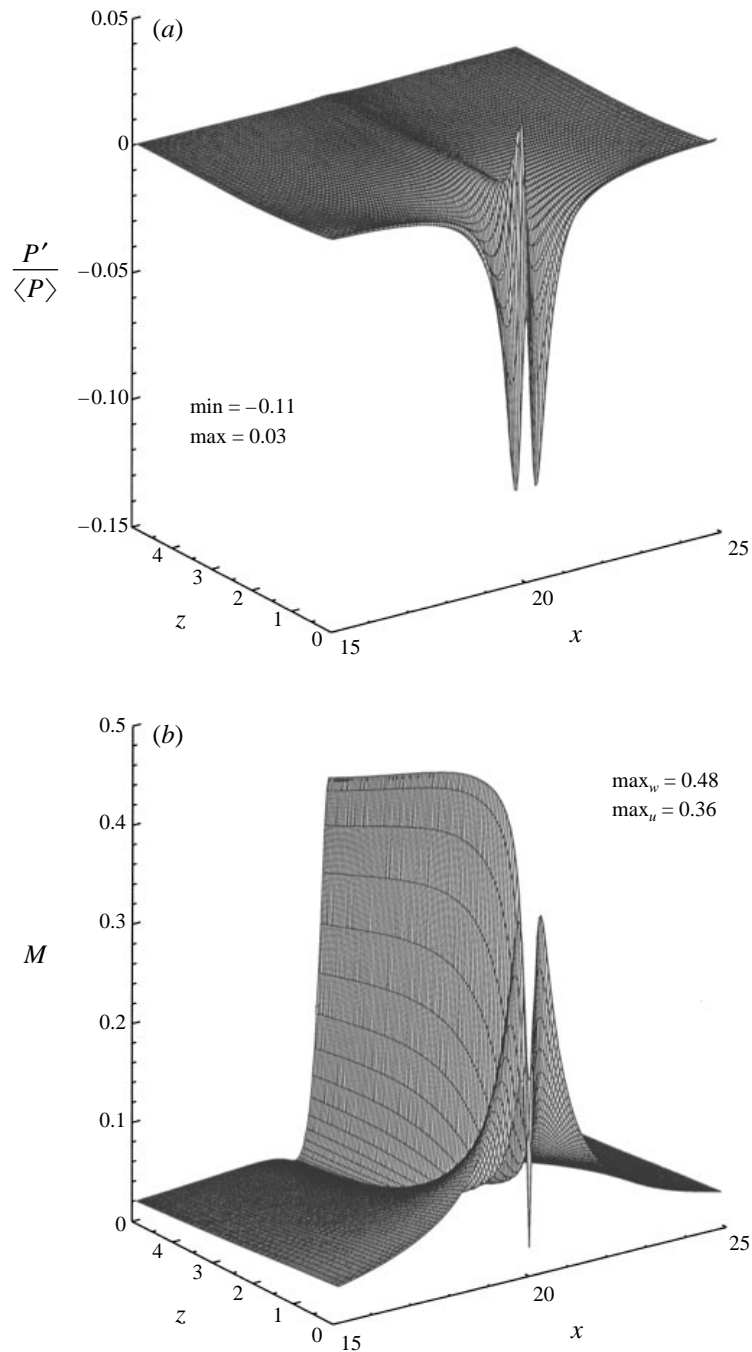


FIGURE 6. Perspective views with depth z and horizontal position x of (a) relative pressure fluctuations $P'/\langle P \rangle$ and (b) flow Mach number M in Case D. Only the central 1/4 and top 1/8 of the computational domain is shown. Horizontal resolution has been reduced by a factor of six for graphic clarity. Also indicated in (a) are the maximum and minimum values of $P'/\langle P \rangle$ and in (b) the maximum vertical and horizontal flow Mach numbers.

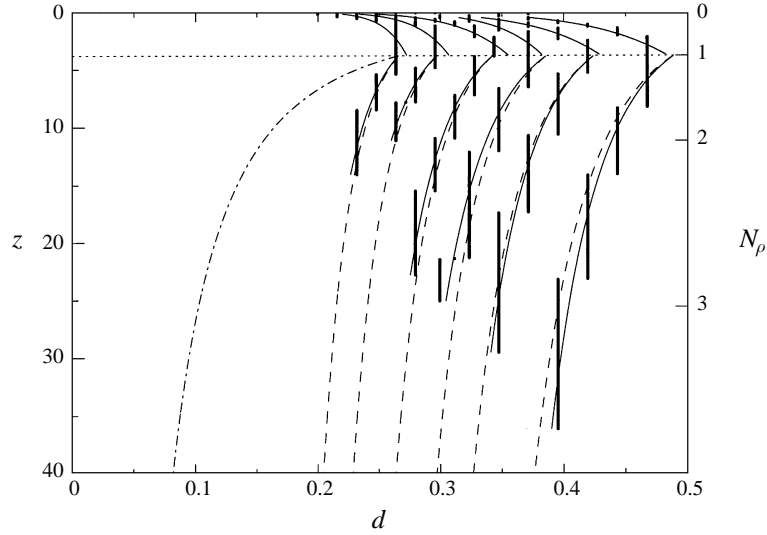


FIGURE 7. Plume stem diameter d , measured as the distance between peak oppositely signed vorticity, as a function of depth z for six experiments of differing fluid viscosity (Series A). Thick vertical bars are composed of individual data points, discontinuities with depth reflect twice the horizontal grid spacing. Thin solid curves plot the best power-law fit to the data and dashed curves indicate scaling-theory behaviour, which in the absence of thermal diffusion predicts $d \sim z^{-1/2}$ (dash-dot curve).

fits to the data. In the topmost scale height the plume stem diameter increases, with the maximum diameter attained scaling empirically as $Re^{-1/2}$. This increase is opposite to the decrease in diameter above one scale height predicted by stratified but incompressible plume models which assume a hydrostatic pressure distribution (Rieutord & Zahn 1995). It is here the result of the large amplitude dynamical pressure fluctuations in the upper portions of the domain which induce entrainment of fluid into the plume stem.

Below the uppermost scale height dynamical pressure fluctuations in the laminar stem flow are small, and the flow properties vary in response to the mean stratification through which the plume descends. Vertical force balance then ensures a decrease in plume diameter with depth, as it would in the simplified hydrostatic plume models if there were no entrainment (in such models an entrainment rate proportional to the mean vertical velocity is generally assumed). The decrease in plume diameter in these simulations can be understood as follows. The primary vertical force balance for the low Prandtl number nearly steady plume stem flows is between buoyancy and horizontal viscous dissipation in the stem core and between buoyancy and horizontal advection immediately outside the core. At the location of vorticity amplitude maximum, which determines our measure of plume diameter, all three force terms are of comparable magnitude,

$$\rho u \frac{\partial w}{\partial x} \sim \rho' g \sim \frac{1}{Re} \frac{\partial^2 w}{\partial x^2}. \quad (11)$$

This implies a plume stem diameter which scales as

$$d^4 \sim \frac{z}{\rho Re^2 \rho' g}. \quad (12)$$

For an adiabatic descent of fluid and small pressure fluctuations ρ'/ρ is approximately

constant, implying that, since $\rho \sim z^{3/2}$ in the background, the plume stem diameter should scale with depth as

$$d \sim z^{-1/2}. \quad (13)$$

That scaling is plotted in figure 7 with a dash-dot line and is steeper than the results found for the numerical experiments. As discussed previously, however, the actual thermodynamics of the fluid descent in these experiments is not adiabatic. The plumes suffer horizontal heat losses even at very low values of thermal conductivity. The scaling of this loss with depth cannot be determined directly from the energy equation. The primary energy balance is between the vertical advection of cool fluid and its heating by compression. Thermal diffusion serves to balance the small remaining difference. A correction to the diameter can however be made empirically by measuring the scaling of diffusive heat losses with depth (found to be about $z^{-1/3}$). From this, the scaling of T' and thus ρ' in (12) can be determined. The dashed lines in figure 7 indicate how well the scaling theory then fits the data. Before the onset of instability and if corrected for broadening by thermal diffusion, the stem flows below one density scale height balance buoyant acceleration with horizontal advection and viscous dissipation.

3.4. Pinch instability and vortex cap structure

In the formation and detachment of the vortex cap structure at the head of these starting plumes, as in the uppermost scale height of the stem flow, dynamical pressure fluctuations play an important role. Figure 8 traces cap evolution in Case F1 by following the motion as the plume descends. The first column displays contours of vorticity, while the second and third show density and pressure perturbations about the mean state. Positive values are indicated with solid and negative values with dashed curves. The plume emerges from the boundary layer and quickly forms the cap and stem structure (figure 8a) familiar from other settings (cf. Moses *et al.* 1993 and references therein). Subsequent evolution is however quite different from that of incompressible plumes. As the fluid in the cap spins up, density fluctuations in the vortex cores become negative (figure 8b). This is because the vortex pair resists compression at the background adiabatic rate and thus, as it descends, quickly finds itself less dense than the surroundings. Ultimately with further descent vortex core densities get so low compared to the background mean value that the integrated buoyancy force on the pair (most easily measured well after head detachment when the identity of the pair can be clearly determined) is actually upward, an example of what Parker (1991, see also Arendt 1993) has called dynamical buoyancy. What keeps the pair propagating downward is the top-to-bottom pressure gradient induced across it as it was spun up. This same dynamical pressure causes secondary head formation within the stem (figures 8c and 8d). The sequence repeats itself, consecutively pinching off vortex pairs each weaker than the previous one and travelling downward through the layer slower than those ahead. Note that this scenario is slightly altered at high Pr . For Prandtl numbers greater than ~ 1 density fluctuations in the vortex core remain positive. This is both because the vorticity of the pair is lower and because the magnitude of the temperature fluctuations within the cap increase under the conditions of low thermal dissipation. Despite these differences dynamic pressure fluctuations behind the cap still initiate secondary head formation and successive vortex pair detachment.

In figure 9 we trace the pinch development in time for two low Pr solutions, Cases D and F1, by plotting, as a function of depth, the separation between peak

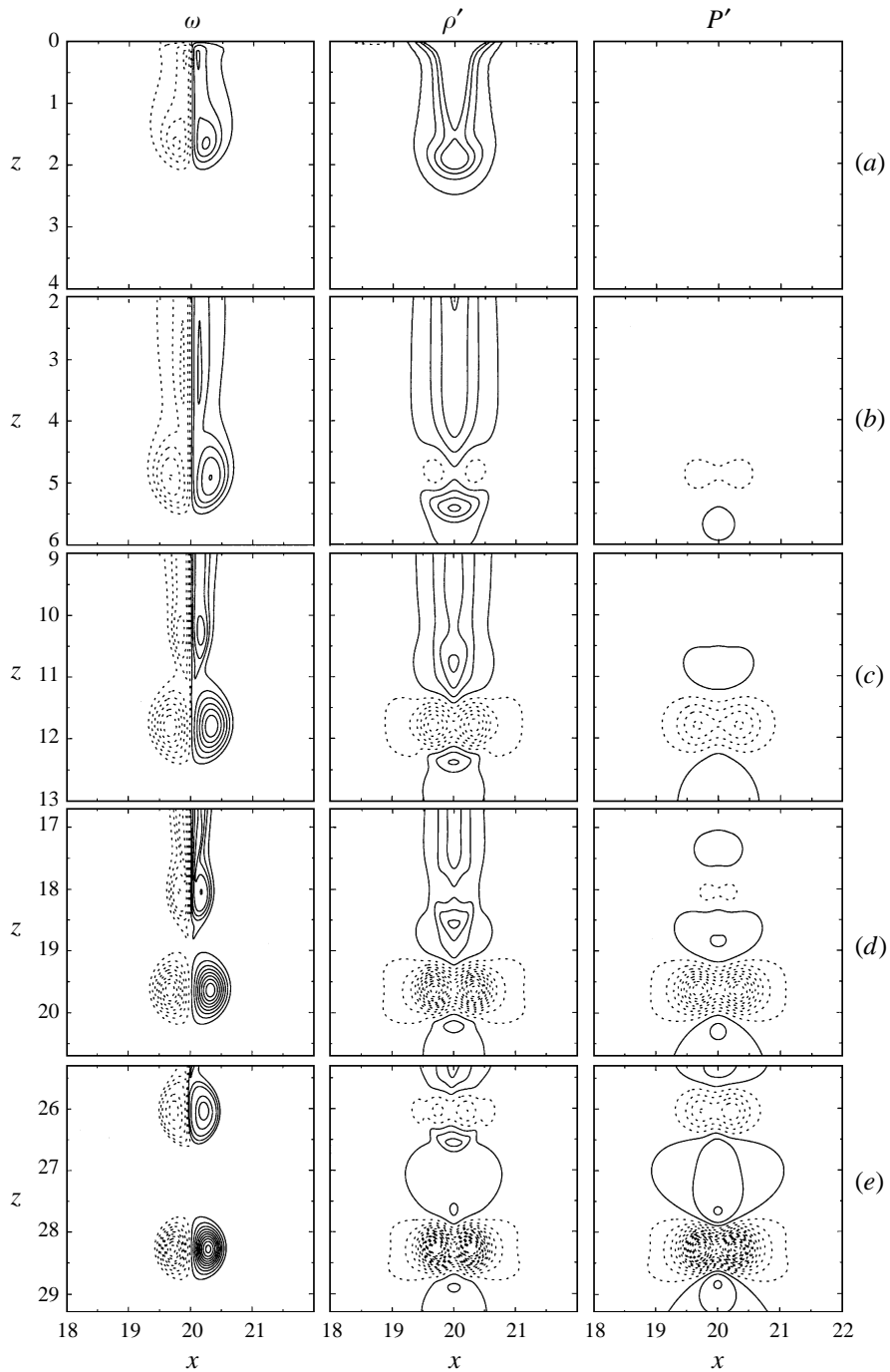


FIGURE 8. Plume cap evolution following the motion. The first, second and third columns display contours of vorticity ω , density fluctuations ρ' , and pressure fluctuations P' respectively. Positive values are indicated with solid and negative values with dashed contours, and all contours for an individual column are scaled by the minimum and maximum of the bottom row. Rows (a)–(e) correspond to times $t = 10.2, 19.5, 36.4, 55.3,$ and 76.0 in Case F1.

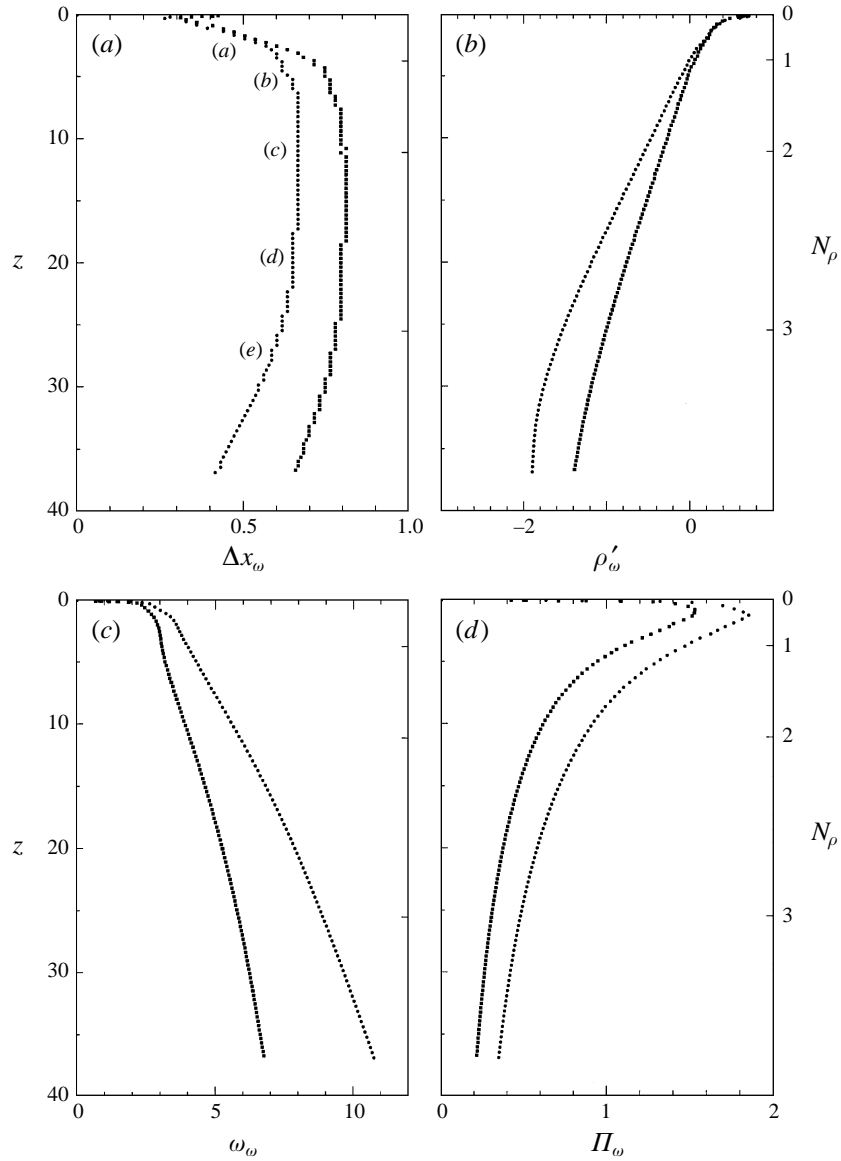


FIGURE 9. Plume cap properties measured at the position of maximum vorticity for Cases D (filled squares) and F1 (filled circles): (a) separation between peak cap vorticity values Δx_ω , (b) density perturbations ρ'_ω , (c) vorticity ω_ω , and (d) potential vorticity Π_ω . Small letters in (a) correspond to the rows of figure 8.

oppositely signed vorticity values in the starting plume cap Δx_ω , and the values of density perturbation ρ'_ω , vorticity ω_ω , and potential vorticity Π_ω ($\Pi = \omega/\rho$) at the location of maximum cap vorticity. These cases have equal Péclet numbers but differing Reynolds numbers. Since the fluid in Case D is more viscous than that in Case F1 (see table 1), dynamic pressure fluctuations develop more slowly and the onset of the pinch instability is delayed. In both cases the separation between peak oppositely signed vorticity values initially increases as the head is formed and then holds a nearly constant value so long as it remains attached to the stem (figure 9a).

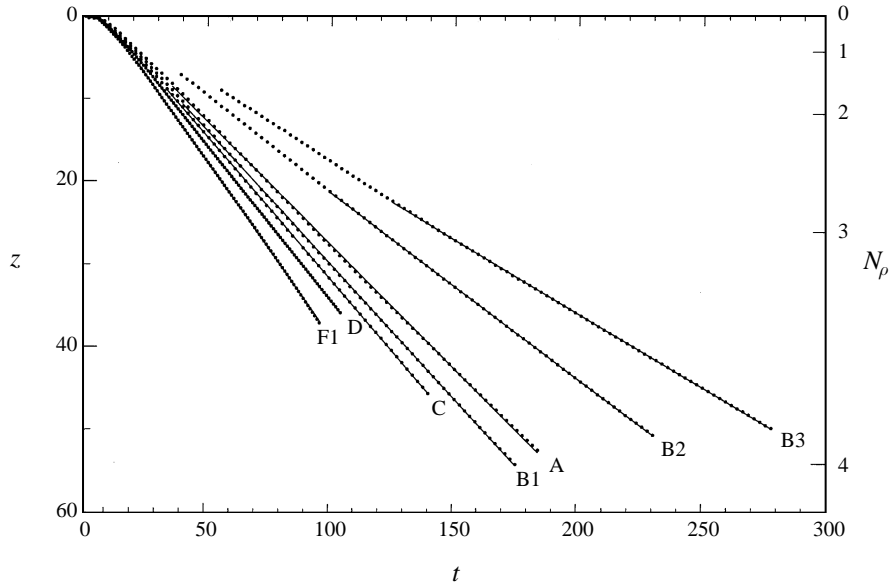


FIGURE 10. Plume cap depth (depth of peak vorticity value) as a function of time t for the simulations indicated by the adjacent case identification. Missing points at shallow depths for high Prandtl number Cases B2 and B3 are due to the cap vorticity not yet being in a well-defined vortex pair. Solid lines plot the best linear fit from the end of head growth, through head detachment, to the end of the run.

Once detachment occurs, the vortex pair is compressed and reduced in size. Below a depth of about one density scale height and until head detachment occurs ρ'_ω decreases linearly, and density fluctuations at the location of peak vorticity (figure 9b) are negative throughout most of the layer. After detachment compression of the pair slows this decrease in ρ'_ω , and in some deeper simulations a reversal can occur with an increase of ρ'_ω in the deepest layers.

Figure 9(c) plots the peak value of vorticity in the cap as a function of depth, and while this quantity steadily increases, dissipation is evident in the decrease of potential vorticity following the initial formation period (figure 9d). The vortex cap structure is fundamentally a viscous one, forming as a result of viscous stress at the plume tip. Lower viscosity results in a smaller initial cap diameter (figure 9a). Additionally, compression with depth of an already formed vortex pair does not result in an increase in the propagation velocity, as would be expected for two point vortices whose separation decreases (e.g. Lamb 1945; Batchelor 1967). Instead, compression of the extended pairs created by these plumes results in viscous dissipation, reduction in the net circulation, and a constant velocity of pair propagation. Figure 10 plots the position of the cap (depth of peak vorticity value) as a function of time. Superimposed is the best linear fit to the points following cap formation. While there is evidence for weak vortex pair acceleration at low Prandtl numbers and deceleration at high, propagation velocities are remarkably constant with depth, scaling empirically with Reynolds and Prandtl numbers as $Re^{0.30}/Pc^{0.23}$.

The cap dynamics can be summarized as a three-stage process: an initial conversion of buoyancy to vorticity by viscous stresses, detachment and propagation due to consequent dynamic pressure perturbations, and ultimate compression and dissipation. Note that the pinch instability manifest in this process is not a varicose mode of the

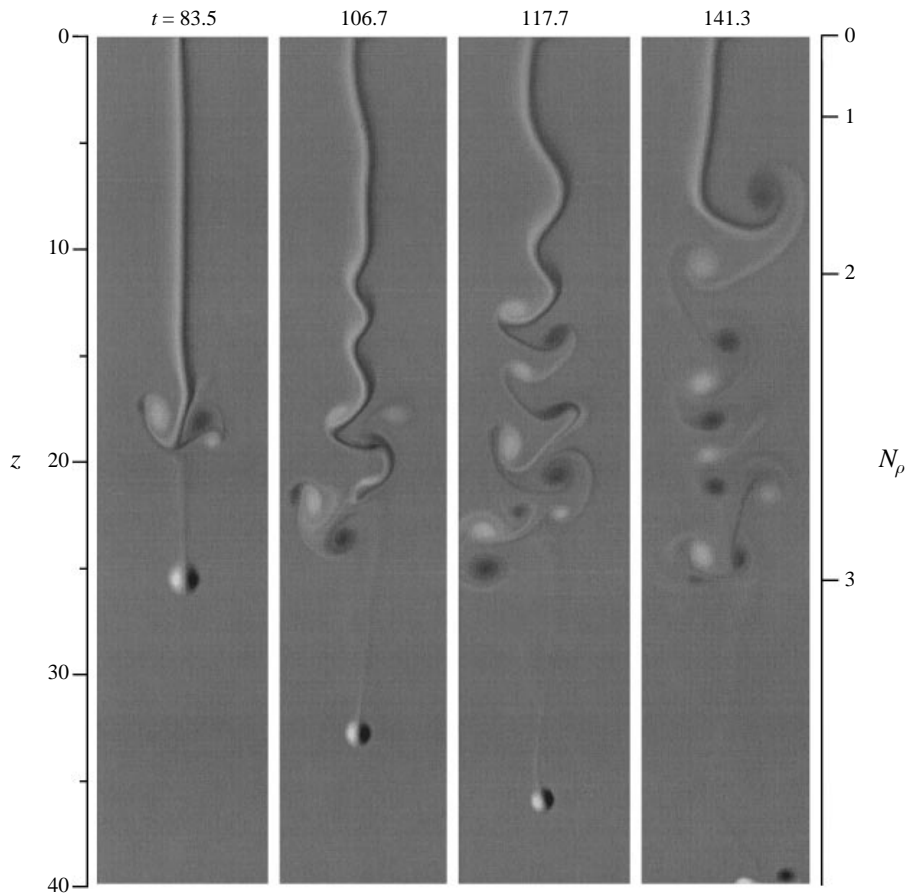


FIGURE 11. A series of horizontal vorticity images (light and dark being oppositely signed vorticity) illustrating the sinuous stem flow instability for Case B1, here computed in a smaller 40×40 domain with uniform gridding. Long-time evolution could thus be followed with vigorous flow extending outward from the central plume region (see figure 15) at the cost of slightly lower than typical resolution. The full vertical extent and $1/5$ the horizontal extent (8 units) of the computational domain is shown in each image.

stem shear flow, which probably grows slower than the sinuous mode to be discussed in the next subsection. Instead it is an intrinsically nonlinear process requiring large local dynamical pressure fluctuations produced by Reynolds stresses.

3.5. Sinuous instability of the stem shear flow

In addition to the pinch instability, these downflowing compressible plumes are subject to a sinuous shear mode. Figure 11 displays a time series of images of the horizontal vorticity for Case B1, here computed in a smaller 40×40 domain with uniform gridding (1024×1024 grid points, resolution $\Delta x = \Delta z = 3.91 \times 10^{-2}$ throughout) and subject to random initial background temperature perturbations of amplitude 10^{-3} . Kelvin–Helmholtz instability of the stem shear flow develops, its onset enhanced by the background noise and occurring before the second pinch. The stem is disrupted, with the long-term behaviour, beyond the time shown in figure 11, being a quasi-

periodic wagging of the remaining stem portion and the shedding of alternately opposite signed vortices at a depth of about $1.5\text{--}2.0N_\rho$.

To understand this instability more fully, we analyse the linear stability of the nonlinear flow realized in our two-dimensional simulation. Fundamental difficulties are associated with such an analysis. The underlying flow is non-parallel, time-dependent, and subject to mean gradients in the direction of motion. We avoid these difficulties by examining the local stability of the plume-stem shear flow at each depth under the assumption that to lowest order the flow at that depth is steady and parallel. Together with side boundary conditions of vanishing velocity such an assumption implies that the unperturbed horizontal velocity must be taken to be identically zero. The magnitude of the actual horizontal velocity in the region of the two-dimensional simulation being considered thus provides a check on the accuracy of this parallel-flow approximation. Measured in the nonlinear solution, as depicted in the first image of figure 11, the maximum horizontal velocity is less than 10% of the maximum vertical velocity for depths between $z = 3$ and 15, and less than 5% of the maximum vertical velocity for depths between $z = 6$ and 14. Above $z = 1.0$, however, maximum horizontal velocities are better than 25% of maximum vertical velocities, even exceeding them in the very upper layers ($z < 0.15$), invalidating the parallel-flow assumption. We thus restrict the linear stability analysis to that region of the domain between $z = 1$ and $z = 15$, with the results most useful below $z \approx 5$.

We solve the linearized equations by Newton–Raphson–Kantorovich iteration (Cash & Moore 1980) for a series of one-dimensional stability problems, where for each the background state is taken from the two-dimensional simulation at a particular depth. The perturbation eigenfunctions are strongly confined to the plume shear layer located far from the influence of the domain sidewalls. The vanishing velocity boundary conditions are thus a good approximation to free-stream conditions in which perturbations decay exponentially with distance. For our local analysis, layer by layer, to be meaningful the vertical disturbance wavelength should be small compared to the depth over which the background varies. We find that this condition is satisfied in our study of Case B1 for depths greater than about $z = 2.5$. At such depths the wavelength of the fastest growing mode is shorter than both the density and pressure scale heights (figure 13*b*). Note that treating each depth separately also requires that gravity be ignored in obtaining the perturbation solution. Otherwise spuriously growing modes are found that extract energy from the mean state even in the absence of shear. Our analysis thus corresponds to examining the linear stability of an unbounded two-dimensional viscous compressible jet, where the jet profile is given by the nonlinear thermal-plume solution at each depth.

The results, when applied to the nonlinear solution illustrated by the first image of figure 11, are summarized by figures 12 and 13. Figure 12 plots the growth rate β_i , phase speed $v_p = \beta_r/\alpha$, and group velocity $v_g = \partial\beta_r/\partial\alpha$ of the linear modes as a function of vertical wavenumber α at three depths. These curves are similar to those obtained for the sinuous modes of more idealized jets (cf. Drazin & Reid 1981) with the exception that the phase and group velocities become negative at very low values of α . This can be understood, remembering that the velocity profiles studied here have a negative (upflowing) region surrounding the downflowing core. At low vertical wavenumbers the eigenfunctions peak in and sample predominantly this outer region. Figure 13 plots β_i , v_p , v_g , and the disturbance wavelength λ for the fastest growing mode at each depth. While varying slowly with depth the wavelength of the fastest growing mode has a value between about 2.1 and 2.7. This is in good qualitative agreement with the wavelength apparent at the onset of instability in the

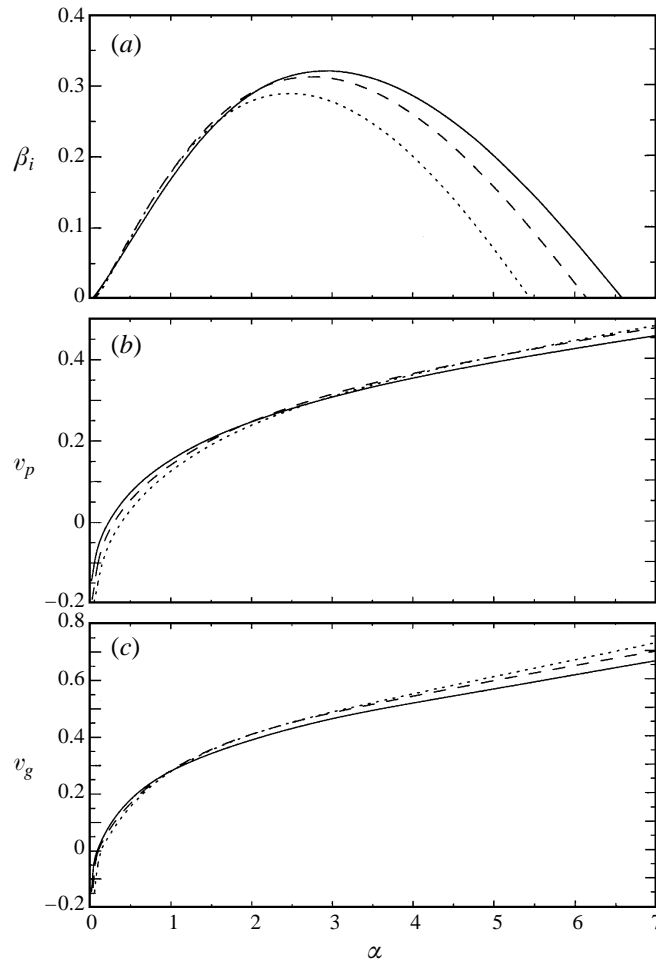


FIGURE 12. Linear stability properties of the stem shear flow illustrated by the first image of figure 11 at three depths: $z = 15$ (solid curve), $z = 10$ (dashed curve), and $z = 5$ (dotted curve): (a) the growth rate β_i , (b) the phase speed v_p , and (c) the group velocity v_g as a function of vertical wavenumber α .

two-dimensional simulation, as illustrated by the second panel of figure 11. Also in good agreement is the fact that the group velocity of the fastest growing mode in the linear problem is approximately equal, at each depth, to the value of the vertical velocity at the inflection point of the nonlinear flow. Additionally, the phase speed of the linear disturbance is less than the group velocity implying an apparent upward propagation of the disturbance phase relative to the flow. This is visually apparent in animated sequences of images of the nonlinear solution. The sinuous instability manifest in the two-dimensional nonlinear simulations thus appears to be a convective linear shear-mode of the underlying stem flow.

An attempt to understand the depth to which the plume stem flow remains stable at late times by such an analysis is a bit more problematic. As already mentioned, following the instability depicted by figure 11, a quasi-periodic shedding of alternately signed vorticity from an apparently stable truncated stem occurs at depth of $z = 5$ – 10 . Considering the convective nature of the instability discussed above, one might suggest a relevant depth scale of $d = v_g/\beta_i$. This is the depth to which the instability

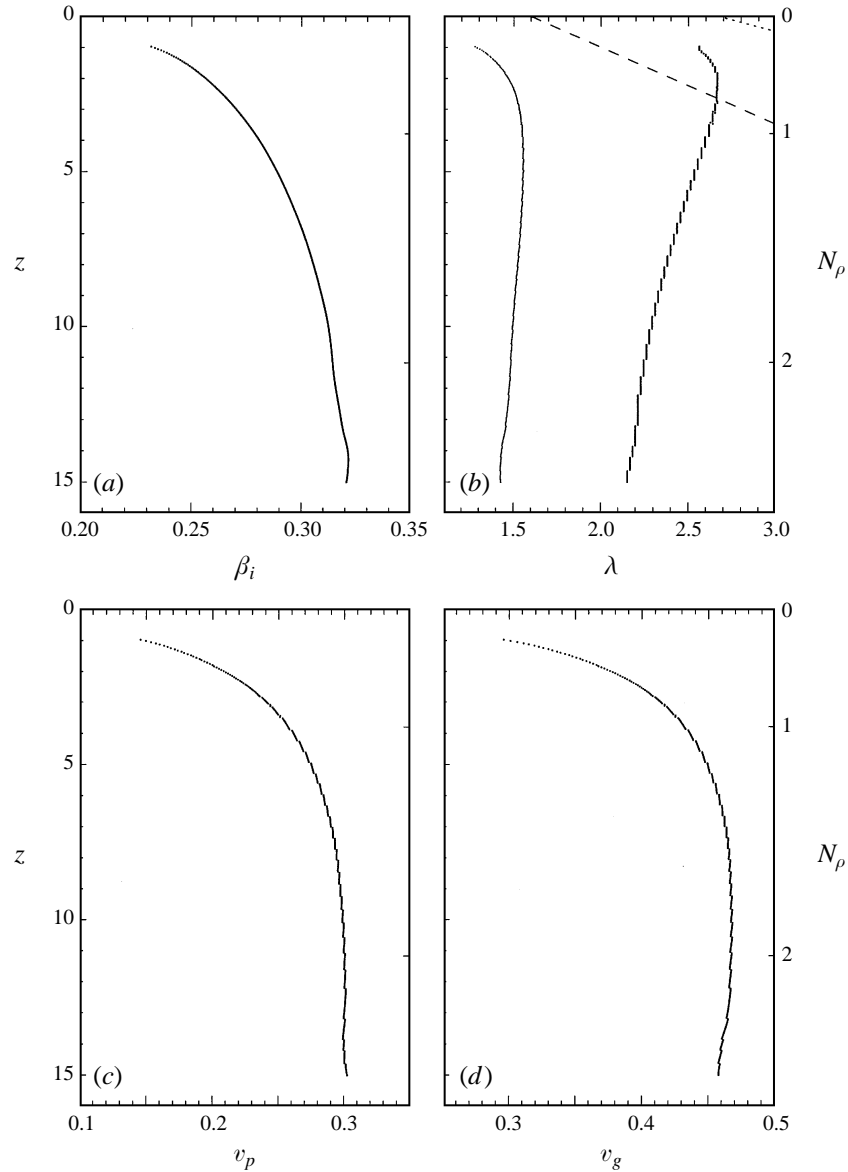


FIGURE 13. Linear stability properties of the fastest growing mode as a function of depth z in the stem shear flow illustrated by the first image of figure 11: (a) the growth rate β_i , (b) the vertical wavelength, (c) the phase speed v_p , and (d) the group velocity v_g . Also plotted in (b) are the density scale height H_ρ (dotted curve), the pressure scale height H_p (dashed curve), and the distance v_g/β_i (thin solid curve). Apparent discontinuities with depth in λ , v_p and v_g reflect the discrete set of wavenumbers chosen for the linear stability calculation.

is convected by the flow before growing appreciably. As illustrated by the thin solid curve in figure 13(b), the value of v_g/β_i for this case is approximately 1.5 over much of the domain. The discrepancy between this value and the apparent stability of the nonlinear solution to five times that depth is perhaps not surprising given that the actual flow is nonlinear, and that both the local analysis and parallel-flow assumptions of the linear problem break down at shallow depths.

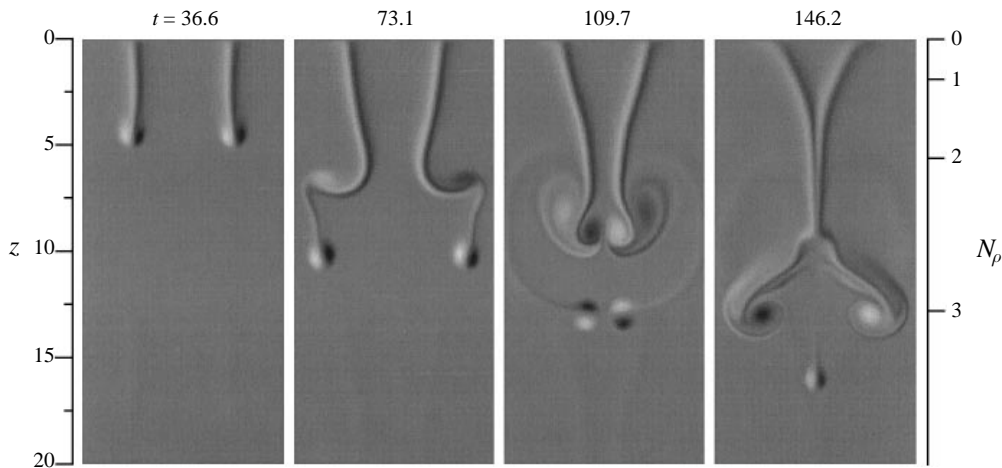


FIGURE 14. A series of horizontal vorticity images (light and dark being oppositely signed vorticity) illustrating the interaction and merger of two identical compressible starting plumes. One half the horizontal extent (10 units) and the full vertical extent of the computational domain is shown.

4. Multiple plumes, upward-directed plumes, and more fully developed flows

In this section we briefly contrast the single downflowing plume discussed above with two comparison cases, one in which two identical starting plumes are driven from the upper boundary, and another in which a single upflow plume is driven from the lower boundary.

A typical two-plume solution is illustrated in figure 14 with a series of images of the horizontal vorticity. The plumes are identical, are started simultaneously, and as in single-plume cases descend through an adiabatic background. Early evolution illustrates an attraction between plume stems and a repulsion between their heads. The attraction results from negative pressure fluctuations between the plumes, a consequence of the increased flow velocity there as compared to that outside. Head repulsion occurs in response to convergent horizontal flow and consequent positive pressure fluctuations induced between the two neighbouring and oppositely signed vortices of the two plume caps. Destabilization and rapid detachment of the caps then occurs, followed by merger of the two stems. Subsequent evolution, beyond that illustrated in figure 14, entails consolidation of a single plume stem below a depth of about $z = 10$, new single-cap formation, and the development of the single-plume instabilities previously discussed.

This example of plume interaction is a rather special case. The plumes are identical, co-temporal, and two-dimensional. These, probably most significantly the two-dimensionality of the flow, clearly restrict the interactions possible, and further study relaxing such restrictions is essential. In particular, it is important to investigate whether plume–plume interactions serve to destabilize the flow, as suggested here, or whether entwining of individual plumes in three dimensions can render them more robust and thus more likely to coherently descend to greater depths. It is clear that the outcome probably depends on the relative signs of the vertical vorticity of the plumes. What is less clear is the role of compressibility in such interactions and its manifestation in secondary instability.

Figure 15 contrasts the evolved flow of an upflowing and downflowing compressible

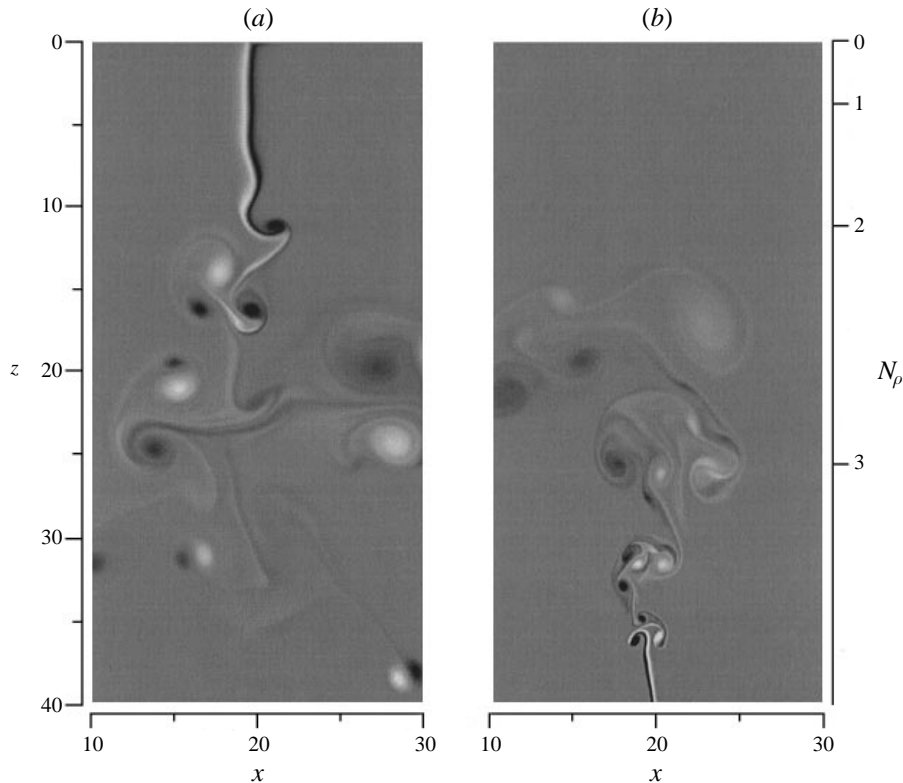


FIGURE 15. Instantaneous horizontal vorticity for two separate experiments, showing (a) the same downflow plume as that in figure 11 at a later time, $t = 329$, and (b) an upflow plume of comparable strength in the same adiabatic background. One half of the horizontal extent (20 units) and the full vertical extent of the computational domain is shown.

plume. The downflow plume depicted is the same as that in figure 11 at a later time ($t = 329$). The plumes are of comparable strength and both backgrounds are adiabatically stratified. Flow development in the two cases is quite distinct. The upflow plume is not subject to the pinch instability. Dynamic pressure fluctuations behind the head are weak due to the expansion of the rising vortex pair. Additionally, if the background is quiescent no sinuous instability is observed, since expansion tends to smooth fluctuations. The sinuous mode can however be realized by inducing asymmetries in the flow with low-amplitude random temperature fluctuations in the initial conditions. For both cases illustrated by figure 15 such fluctuations of amplitude 10^{-3} were introduced. The upflowing stem flow is consequently unstable with height and vortex pairs are shed into the domain above. The pairs expand and slow as they rise, with successive pairs travelling faster, penetrating and disrupting the previous one as in the familiar leap-frogging of two vortex rings seen in laboratory experiments (Yamada & Matsui 1978). As a result the fluid, rather than moving out of the plume region as a series of detached vortex pairs, as seen in the compressible downflowing plume, is wrapped back into the upflowing plume region. The whole region expands with height within a roughly conically shaped envelope reminiscent of incompressible turbulent plumes. Note that the region of significant vortex interaction for the downflowing plume of figure 15 (between depth of $z = 15$ and 30) reflects the ensemble of vorticity shed by the initial onset of sinuous stem instability (figure 11)

not the interaction of individual vortex pairs. Individual vortex pairs shed by the downflowing plume prior or subsequent to that event leave the plume region as entities.

These results suggest a fundamental distinction between the dynamics of upflowing and downflowing plumes in a stratified medium. A downflowing plume in such a setting sheds vorticity which leaves the plume region, descends through the medium, and remains compact due to compression with depth. Interactions between compact vortex pairs shows little large-scale organization. An upflowing plume, by contrast, sheds vortex pairs which expand and slow as they rise. Subsequent interactions tend to wrap the vorticity back into the larger plume structure. These dynamical differences suggest that while an entrainment hypothesis may prove useful in describing compressible upflowing plumes in a stratified medium, as it already has for incompressible plumes in a variety of settings (e.g. Turner 1986 and references therein), entrainment may be an inappropriate description of compressible downflowing plume behaviour even under more turbulent flow conditions. The dynamics of compressible downflowing plumes may be better described by the shedding of and interaction between detached vorticity, with the plumes quickly losing their identity with depth. Three-dimensional turbulent compressible plume studies are needed to further address this issue, and such studies are in progress.

5. Conclusion

We have conducted detailed studies of fully compressible two-dimensional thermal starting plumes. When computed at extremely high numerical resolution, such plumes are subject to vigorous secondary instabilities. Dynamical pressure fluctuations play an important role leading to the detachment of compact vortex pairs. These pairs leave the plume region with only limited interaction due to compression in the presence of significant mean stratification. In this section we reconnect this work with its astrophysical motivation, discussing possible implications.

Solar and stellar envelope convection is driven by enormous photospheric radiative losses. Granulation, the manifestation of such convection on the Sun, is surface driven and dominated by new downflow plume formation (Rast 1995, 1998). The work presented in this paper suggests that these downflows are unlikely to be coherent below a few scale heights depth. Compressible downflow plume dynamics is sufficiently different from that of incompressible plume or compressible upflowing plume dynamics that previous estimates of plume size, spacing, and strength at the base of the solar convection zone which depend on simple plume models are likely to be in error. The error results from the assumptions of hydrostatic pressure distribution and velocity proportional entrainment both of which are called into question by our studies. Rather than coherent downflows to the base of the solar convection zone, our studies suggest a surface layer of convection, the dynamics of which is dominated by radiative loss, new downflow plume formation, and plume disruption, overlying a region of perhaps larger scale nearly Boussinesq convection. Understanding an entire shell of highly stratified convection (in the Sun spanning 2×10^5 km with a density scale height in the surface layers of about 350 km) encompassing both these regimes promises great challenge. While computation of the entire layer at resolutions which also allow the complex dynamics of the near surface layers is currently beyond capability, it may be possible to use what is learned about the dynamics, stability, and interaction of individual plumes in the surface layers to provide a dynamical upper boundary condition on a deeper less stratified domain.

Compressible plume studies should be, and currently are being, extended to three dimensions. While it is difficult to imagine how three-dimensionalization would serve to stabilize the flow, it is likely that multiple plume interactions are significantly influenced by the additional spatial freedom. In particular, it is important to determine whether multiple plume coalescence can result in deeper downflow coherence or whether the resulting plume is also then disrupted in short order by secondary instability. Study of thermal plumes in a more realistic setting than that of an adiabatic background is also desirable. It is possible that thermal-plume dynamics is fundamentally different from downflow dynamics in other convecting environments. While we have argued elsewhere (Rast 1995, 1998) that solar granulation, and by analogy convection in the photospheric layers of other stars, can best be understood as the continuous formation of new downflow plumes in response to locally enhanced surface cooling, unequivocal demonstration of the importance of the dynamics discussed in this paper to those settings awaits a significant increase in computational capabilities which would allow for comparable resolution to that achieved here under more realistic flow conditions.

Special thanks to S. Arendt, T. Bogdan, N. Brummell, F. Cattaneo, P. Charbonneau, T. Emonet, K. Julien, K. MacGregor, S. Tobias, and J. Werne.

REFERENCES

- ARENDRT, S. 1993 On the dynamical buoyancy of vortices. *Astrophys. J.* **412**, 664–674.
- BATCHELOR, G. K. 1967 *An Introduction to Fluid Dynamics*. Cambridge University Press.
- CASH, J. R. & MOORE, D. R. 1980 A high order method for the numerical solution of two-point boundary value problems. *BIT* **20**, 44–52.
- CATTANEO, F., BRUMMELL, N. H., TOOMRE, J., MALAGOLI, A. & HURLBURT, N. E. 1991 Turbulent compressible convection. *Astrophys. J.* **370**, 282–294.
- CHARBONNEAU, P. & MACGREGOR, K. B. 1997 Solar interface dynamos. II. Linear, kinematic models in spherical geometry. *Astrophys. J.* **486**, 502–520.
- COX, J. P. & GIULI, R. T. 1968 *Principles of Stellar Structure*. Gordon and Breach.
- DRAZIN, P. G. & REID, W. H. 1981 *Hydrodynamic Stability*. Cambridge University Press.
- GRAHAM, E. 1977 Compressible convection. In *Problems of Stellar Convection, IAU Colloquium 38, Nice 1976* (ed. E. A. Spiegel & J.-P. Zahn), pp. 151–155. Springer.
- HURLBURT, N. E., TOOMRE, J. & MASSAGUER, J. M. 1984 Two-dimensional compressible convection extending over multiple scale heights. *Astrophys. J.* **282**, 557–573.
- LAMB, H. 1945 *Hydrodynamics*. Dover.
- MASSAGUER, J. M. & ZAHN, J.-P. 1980 Cellular convection in a stratified atmosphere. *Astron. Astrophys.* **87**, 315–327.
- MOSES, E., ZOCCHI, G. & LIBCHABER, A. 1993 An experimental study of laminar plumes. *J. Fluid Mech.* **251**, 581–601.
- PARKER, E. N. 1991 Dynamical buoyancy of hydrodynamic eddies. *Astrophys. J.* **380**, 251–255.
- PARKER, E. N. 1993 A solar dynamo surface wave at the interface between convection and nonuniform rotation. *Astrophys. J.* **408**, 707–719.
- RAST, M. P. 1991 High wavenumber thermal convection enhanced in regions of partial ionization. In *Challenges to Theories of the Structure of Moderate-Mass Stars* (ed. D. Gough & J. Toomre), pp. 179–186. Springer.
- RAST, M. P. 1992 Compressible convection with ionization. PhD Thesis, University of Colorado.
- RAST, M. P. 1995 On the nature of ‘exploding’ granules and granule fragmentation. *Astrophys. J.* **443**, 863–868.
- RAST, M. P. 1998 Solar granulation: A surface phenomenon. In *Geophysical and Astrophysical Convection* (ed. P. Fox & R. M. Kerr), Gordon and Breach (in press).
- RAST, M. P., NORDLUND, A., STEIN, R. F. & TOOMRE, J. 1993 Ionization effects in three-dimensional solar granulation simulations. *Astrophys. J.* **408**, L53–L56.

- RAST, M. P. & TOOMRE, J. 1993*a* Compressible convection with ionization. I. Stability, flow asymmetries, and energy transport. *Astrophys. J.* **419**, 224–239.
- RAST, M. P. & TOOMRE, J. 1993*b* Compressible convection with ionization. II. Thermal boundary-layer instability. *Astrophys. J.* **419**, 240–254.
- RICHTMYER, R. D. & MORTON, K. W. 1967 *Difference Methods for Initial-Value Problems*. Interscience.
- RIEUTORD, M. & ZAHN, J.-P. 1995 Turbulent plumes in stellar convective envelopes. *Astron. Astrophys.* **296**, 127–138.
- SCHMITT, J. H. M. M., ROSNER, R. & BOHN, H. U. 1984 The overshoot region at the bottom of the solar convection zone. *Astrophys. J.* **282**, 316–329.
- SIMON, G. W. & WEISS, N. O. 1991 Convective structures in the Sun. *Mon. Not. R. Astron. Soc.* **252**, 1p–5p.
- STEIN, R. F. & NORDLUND, A. 1989 Topology of convection beneath the solar surface. *Astrophys. J.* **342**, L95–L98.
- TURNER, J. S. 1986 Turbulent entrainment: the development of the entrainment assumption, and its application to geophysical flows. *J. Fluid Mech.* **173**, 431–471.
- YAMADA, H. & MATSUI, T. 1978 Preliminary study of multiple slip-through of a pair of vortices. *Phys. Fluids* **21**, 292–294.
- ZAHN, J.-P. 1991 Convective penetration in stellar interiors. *Astron. Astrophys.* **252**, 179–188.
- ZOCCHI, G., MOSES, E. & LIBCHABER, A. 1990 Coherent structures in turbulent convection, an experimental study. *Physica A* **166**, 387–407.